Computers and Fluids 136 (2016) 1–10

Contents lists available at ScienceDirect

Computers and Fluids

journal homepage: www.elsevier.com/locate/compfluid

Numerical investigation of electrohydrodynamic instability and bifurcation in a dielectric liquid subjected to unipolar injection☆

Bo-Fu Wang[a,b], Tony Wen-Hann Sheu[b,*]

[a] Shanghai Institute of Applied Mathematics and Mechanics, and Shanghai Key Laboratory of Mechanics in Energy Engineering, Shanghai University, Shanghai 200072, China
[b] Center for Advanced Studies on Theoretical Science, National Taiwan University, Taipei, 106, Taiwan

ARTICLE INFO

Article history:
Received 1 April 2015
Revised 2 March 2016
Accepted 12 May 2016
Available online 12 May 2016

MSC:
00-01
99-00

Keywords:
Unipolar injection
Electroconvective instability
High resolution
Bifurcation
Chaos
Hysteresis

ABSTRACT

The electroconvection of dielectric liquids subjected to unipolar injection is numerically studied in a two-dimensional cavity. To understand the Coulomb force driven electroconvective instabilities and bifurcations in the closed cavity, a high resolution upwind scheme is applied to carry out linear stability analysis and numerical simulation of nonlinear electrohydrodynamic equations. We focus on the strong injection case, where the non-dimensional injection parameter C is fixed at $C = 10$. The length to height ratio of the cavity is fixed at 0.614. The numerical simulations are performed subject to free and rigid lateral wall boundary conditions. Two dimensionless mobility parameters $M = 5$ and $M = 10$ are considered for each kind of the lateral boundary conditions. Our linear stability analysis result is consistent with previous theoretical predictions. The nonlinear behaviors of the investigated system beyond the convection threshold are carefully examined. Abundant bifurcation phenomena, such as the pitchfork bifurcation, Hopf bifurcation, quasi-periodic Hopf bifurcation and heteroclinic bifurcation, have been observed. Some nonlinear flow features, such as the hysteresis loops, coexistence of multiple solutions and transition to chaos, have also been demonstrated. Our simulation results show that flow structure and bifurcation sequence can be greatly affected by the specified lateral boundary conditions and the chosen mobility parameters. Besides the static state, a series of steady and unsteady solutions has been calculated, like the one-cell steady state, one-cell periodic state, one-cell quasi-periodic state, and the one-cell chaotic state. All these convective states with two-cell structure are also obtained. Moreover, a periodic state oscillating between the one-cell structure and the two-cell structure has been found in flow domain bounded by rigid walls.

1. Introduction

Electrohydrodynamics (EHD) is an important subject of studying dynamics of moving electrical charges in liquid fluid flows. In the context of EHD, both of the Coulomb and dielectric forces can give rise to flow motion. In current numerical study, the liquid fluid bounded by a rectangular cavity is subjected to unipolar injection and the dielectric force is considered to be negligibly small. The Coulomb force, on the contrary, in the nonlinear hydrodynamic equations (Navier–Stokes equations) is one of the destabilizing sources capable of making the simulation of electrically charged fluid flows very difficult.

Besides the academic importance of exploring hydrodynamic instability in the two-field coupling nonlinear system and resolving computational difficulties due to the presence of high gradient electric charge density, EHD plays a practically significant role as well in many processing industries [1] and emerging technologies [2]. We are therefore motivated to investigate the unipolar injection in dielectric liquid so as to improve our understanding of the hydrodynamic/electric coupled nonlinear dynamical system in a simple geometry configuration.

Charge motion in gases is fairly fast and is hence weakly coupled with the liquid flow motion. As a result, the one-way coupling of the electric-hydrodynamic equations exists without the gas flow affecting the discharge transport [3]. On the contrary, fluid velocity plays a dominant role in liquids and the charge distribution depends greatly on the liquid velocity. In liquids, a strong coupling of different field equations exhibits a scenario that the liquid motion is subjected to an electric Coulomb force acting on the injected space charge. At the same time, the temporal charge distribution is influenced by convection current density. Study of such a complex coupling between the electrical and hydrodynamical field equations has been the subject of many researches in the past several decades. We have known that the electroconvection in a layer

☆ Fully documented templates are available in the elsarticle package on CTAN.

* Corresponding author. Fax: +886-2-23929885.
E-mail address: twhsheu@ntu.edu.tw (T. Wen-Hann Sheu).

http://dx.doi.org/10.1016/j.compfluid.2016.05.009
0045-7930/

of dielectric liquid subjected to unipolar injection is an analogy to the Rayleigh-Bénard problem [4]. To acquire more knowledge about the critical instability parameters, beyond which linear and nonlinear instabilities set in, is also practically and academically essential.

The previous endeavors were mainly focused on the stability near the convection threshold. Both linear and nonlinear criteria have been well established. The linear stability of a liquid layer of infinite horizontal extent was intensively studied by Schneider et al. [5] and Atten et al. [6]. Later on, the nonlinear stability was investigated by Atten et al. [7] both theoretically and experimentally.

A series of studies of electroconvection in dielectric liquids in a finite two-dimensional enclosed cavity has been recently performed [8–10]. Both rigid and free (symmetry) sidewall boundary conditions are considered in these works. Traoré et al. [8] illustrated the evolution of flow state with the increasing value of driving parameter T under the strong injection case. Wu et al. [9] presented in detail their linear stability, nonlinear stability, and bifurcation studies under a strong unipolar injection. They paid attention to the subcritical behavior and analyzed its dependence on the aspect ratio and lateral boundary condition. Following the Wu et al.'s work, Pérez et al. [10] further studied the linear stability of this system, and they pointed out that the inherent importance of the stability results from the nonlinear flow development.

Only a few experimental studies on unipolar injection have been reported. Atten et al. [11] analysed the strong injection case in a large aspect ratio cavity. They found that subsequent to the onset of instability flow immediately becomes time-dependent and chaotic. Such a time-dependent and chaotic behaviour was also investigated by Malraison et al. [12] experimentally.

So far several methods have been applied to simulate the coupled nonlinear EHD system. As the charge conservation equation is convection dominant, numerical simulation becomes a difficult task. It is especially challengeous to simulate such a class of flows under the strong injection condition and in the presence of a large gradient of charge density. A high-resolution method is therefore required to resolve this problem. In early times, Castellanos et al. [13], Chicón et al. [14] and Vázquez et al. [2] adopted particle-in-cell method, Pérez et al. [15], Vázquez et al. [2] and Vázquez et al. [16] employed flux-corrected transport (FCT) schemes. Recently, the total variation diminishing (TVD) schemes [8,9] are applied as well for performing this simulation. Moreover, discontinuous Galerkin finite element method has been implemented by Vázquez et al. [17] in their calculation. In this work, the upwind scheme of Chertock et al. [18], which can not only satisfactorily tackle the high gradient charge density case but also preserve the positivity of the computed charge density, is applied.

Besides accurately solving the nonlinearly coupled electric and hydrodynamic equations and resolving high gradient solutions, we are in particular interested in studying flow instability and bifurcation in this electroconvection dynamical system. The reason is that electroconvection has a strong relevance to the nonlinear and pattern-formation subjects such as the hysteresis loops, multiple solutions, and chaos. For simplicity, unipolar injection problem is chosen to study in detail the nonlinear behavior of the dielectric liquid immersed in a rectangular cavity. Our aim is to enlighten flow transition from a static solution to a quasi-periodic or chaotic solution.

The rest of this paper is organized as follows. In Section 2, the classical electric/hydrodynamic coupling equations are formulated in detail. The problem under current investigation and its associated boundary conditions are described. In Section 3, the numerical methods, including the numerical simulation method and the linear stability analysis, adopted in the present research are introduced. Verification studies are also given in this section to ensure correctness of the proposed numerical approaches. The results are presented in Section 4. The issues about flow bifurcation with increasing and decreasing of T values are addressed in both cases involving the free and rigid walls. The effects of the mobility parameter on the flow evolution are revealed as well. Finally, some conclusions are drawn in Section 5 based on the simulated solutions.

2. Governing equations

At the zero magnetism limiting condition, the classical Maxwell's equations can be reduced to the following set of equations [19]

$$\nabla \times \boldsymbol{E} = 0, \tag{1}$$

$$\nabla \cdot \boldsymbol{E} = \frac{q}{\varepsilon_0}, \tag{2}$$

$$\frac{\partial q}{\partial t} + \nabla \cdot \boldsymbol{J} = 0. \tag{3}$$

In the above, q is the ion charge density, ε_0 the permittivity of free space, and $\boldsymbol{J}$ the current density. In Eq. (1), one can rewrite the electric field $\boldsymbol{E}$ in terms of the electric potential Φ as follows

$$\boldsymbol{E} = -\nabla \Phi. \tag{4}$$

By substituting the above constitutive equation into Eq. (2), the Gauss law can be expressed in terms of Φ as

$$\nabla^2 \Phi = -\frac{q}{\varepsilon_0}. \tag{5}$$

The motion of ions present in between the two parallel plates results mainly from the convection flow drifted by the electric field and the molecular diffusion. The constitutive law for the current density $\boldsymbol{J}$ can be therefore expressed as the sum of the drift current density $q\mu\boldsymbol{E}$, convection current density $q\boldsymbol{u}$, diffusion current density $-D\nabla q$, and the conduction current density. In other words, $\boldsymbol{J} = q\mu\boldsymbol{E} + q\boldsymbol{u} - D\nabla q + \sigma\boldsymbol{E}$, where μ is the ion mobility, D the ion diffusion coefficient, σ the ion conductivity, and $\boldsymbol{u}$ the fluid velocity [19]. Among the above different mechanisms possibly resulting in an ion motion, the diffusion current is comparatively small and can be neglected, at least, under weak injection condition [20]. Both of the magnetic effect and Joule heating are negligible as the current is generally very weak in the assumed perfectly insulting liquids. The conductivity in present study is also assumed to be negligibly small for the same reason. The presence of the term $q\boldsymbol{u}$ in the total flux vector $\boldsymbol{J}$ implies that dielectric flow can modify electric field through the ion-convection effect. In this study the hyperbolic equation given below is adopted to account for the current continuity

$$\frac{\partial q}{\partial t} + \nabla \cdot [q\,(\mu\,\boldsymbol{E} + \boldsymbol{u})] = 0. \tag{6}$$

By expanding the second term shown in the above equation, one can easily get $\nabla \cdot [\, q\,(\mu\,\boldsymbol{E} + \boldsymbol{u})] = \nabla\, q \cdot (\mu\,\boldsymbol{E} + \boldsymbol{u}) + \frac{\mu\, q^2}{\varepsilon_0}$. The resulting current continuity equation given below for the transport of ion charge density becomes nonlinear

$$\frac{\partial q}{\partial t} + \nabla\, q \cdot (\mu\,\boldsymbol{E} + \boldsymbol{u}) + \frac{\mu\, q^2}{\varepsilon_0} = 0. \tag{7}$$

Owing to the velocity vector $\boldsymbol{u}$ shown in the limiting Maxwell's equations, the electric field equation should be solved together with the hydrodynamic equations for the closure reason. The problem under current investigation becomes therefore the subject of electrohydrodynamics. The fluid under investigation is assumed to be isothermal and incompressible with a constant density ρ. Under these assumptions, the hydrodynamic equations for the velocity

vector $\boldsymbol{u}$ and the pressure p are governed by the respective mass conservation equation and the nonlinear momentum conservation equations given below

$$\nabla \cdot \boldsymbol{u} = 0, \tag{8}$$

$$\frac{\partial \boldsymbol{u}}{\partial t} + \boldsymbol{u} \cdot \nabla \boldsymbol{u} = -\frac{1}{\rho} \nabla\, p + \nu \nabla^2 \boldsymbol{u} + \boldsymbol{f_e}. \tag{9}$$

In the above, ν ($\equiv \eta/\rho$) and η denote the kinematic viscosity and the dynamic fluid viscosity, respectively. For the body force $\boldsymbol{f_e}$ it can be generally expressed as follows [21]

$$\boldsymbol{f_e} = \frac{1}{\rho} \left\{ q\, \boldsymbol{E} - \frac{1}{2} (\boldsymbol{E} \cdot \boldsymbol{E}) \nabla \varepsilon + \frac{1}{2} \rho \nabla \left[\left(\frac{d\varepsilon}{d\rho} \right)_{\theta}\ \boldsymbol{E} \cdot \boldsymbol{E} \right] \right\}. \tag{10}$$

In the above, θ is the absolute temperature. The first term, or the Coulomb force term [22], is generated as the result of an established electric field $\boldsymbol{E}$ that is exerted on the charge of volume (or surface) density q. The bulk force $q\boldsymbol{E}$ plays a destabilizing role and has strong association with the coincident onset of flow convection and instability [12]. The second term called as the dielectric (or dielectrophoretic) force term is generated owing to the permittivity gradient and can give rise to a permanent flow motion [23]. This force is normally weaker than the Coulomb force except in conditions when the AC electric field with a very high frequency is applied [4]. In this study, the permittivity is assumed to be uniform everywhere and the dielectric force, which is $-\frac{1}{2}(\boldsymbol{E} \cdot \boldsymbol{E}) \nabla \varepsilon$, has no effect on the electroconvection. The last term, which is called as the electrostrictive term, is nearly diminishing under the uniform permittivity condition. As a result, the equations to be investigated for the velocity vector $\boldsymbol{u}$ is derived as:

$$\frac{\partial \boldsymbol{u}}{\partial t} + \boldsymbol{u} \cdot \nabla \boldsymbol{u} = -\frac{1}{\rho} \nabla\, p + \nu \nabla^2 \boldsymbol{u} + \frac{1}{\rho}\, q\, \boldsymbol{E}. \tag{11}$$

In the presence of Coulomb force distributed in the bulk of fluids, the liquid is normally set into motion. Such a flow motion can change charge density distribution and alter electric field. The complex nonlinear coupling between two sets of equations makes the numerical investigation of electrohydrodynamics a difficult task. Note that $\boldsymbol{u} = 0$ is the trivial solution of Eq. (11)[23,24]. The Coulomb repulsion, which can result in an unstable charge distribution between the parallel electrodes, tends to destabilize the motionless state [11]. Because of this instability issue, we need to know under what condition the flow field with the trivial solution $\boldsymbol{u} = 0$ becomes destabilized. Depending on an infinitely small or a finite ionic drift velocity, which is defined as $\mu \cdot E$, two types of physical instability may occur. Linear instability is related to an infinitely small ionic drift velocity while the nonlinear instability has association with a finite amplitude velocity [11]. These two instability criteria have been obtained respectively through the linear instability analysis [6] and from the nonlinear instability analysis [7] on the currently investigated unipolar injection problem. We will focus on the instabilities and bifurcations during flow transition from static to complex flow states.

The two-dimensional electrohydrodynamic differential system comprises seven equations for the field variables u, v, p, Φ, q, E_x and E_y. They will be normalized for the sake of general application. The characteristic quantities for these unknowns are chosen to be Φ_0 for Φ, Φ_0/d for $\boldsymbol{E}$, $\mu\, \Phi_0/d$ for $\boldsymbol{u}$, $\rho\, \mu^2\, \Phi_0^2\, /d^2$ for p and q_0 for q. Two sets of the independent variables (x, y) and t are normalized by the characteristic length d and the drift time τ_d ($\equiv d^2/\mu\, \Phi_0$), where d is the height of the physical domain.

Besides the drift time, the other two time scales have been known to be able to normalize time [16]. In contrast to τ_d, which is related to the velocity distribution, these time scales have close association with the charge distribution. They are known as the viscous time scale τ_ν ($\equiv \frac{d^2}{\nu}$) and the Coulomb repulsion time scale τ_C ($\equiv \frac{\varepsilon}{\mu\, q_0}$). In this study the time scale τ_d is chosen since it is more suitable for us to describe the EHD equations [2]. The injection strength parameter C, which is considered as an appropriate measure of the injection strength or level, is defined as

$$C = \frac{q_0\, d^2}{\varepsilon\, \Phi_0}. \tag{12}$$

Given the above characteristic quantities for the dependent as well as the independent variables, all the working equations can be transformed to their corresponding dimensionless equations as follows for the electric field equations given in (13)–(15) and the hydrodynamic transport equations given in (16)–(17)

$$\nabla^2 \Phi = -Cq, \tag{13}$$

$$\boldsymbol{E} = -\nabla \Phi, \tag{14}$$

$$\frac{\partial q}{\partial t} + \nabla \cdot [\ q\ (\boldsymbol{E} + \boldsymbol{u})\ ] = 0, \tag{15}$$

$$\nabla \cdot \boldsymbol{u} = 0, \tag{16}$$

$$\frac{\partial \boldsymbol{u}}{\partial t} + (\boldsymbol{u} \cdot \nabla)\, \boldsymbol{u} = -M^2 \nabla\, p + \frac{M^2}{T} \nabla^2 \boldsymbol{u} + CM^2\, q\, \boldsymbol{E}. \tag{17}$$

Two control parameters in the dimensionless EHD dynamical system are defined as $T = \frac{\varepsilon\, \Phi_0}{\rho \nu\, \mu}$ and $M = \frac{1}{\mu}\ (\frac{\epsilon}{\rho})^{\frac{1}{2}}$. The dimensionless parameter T is named as the electric stability parameter [23]. It formally represents the ratio of the Coulomb force and the viscous force. In unipolar injection, the bulk Coulomb force is normally generated by the unstable space charge density distribution. The mobility parameter M represents the ratio of the hydrodynamic mobility and the ion mobility [2,16]. This parameter is important because of its pertinence to characterize a fully turbulent electroconvection induced by charge injection [20]. It is worthy to note here that $T/M^2 = Re_E$. The electric Reynolds number Re_E ($\equiv \frac{\mu\, \Phi_0}{\nu}$) can be therefore used to measure the degree of nonlinearity in the electroconvective system. A larger value of T/M^2 shown in Eq. (17) corresponds to an EHD dynamical system of higher nonlinearity. According to Eq. (17), the Coulomb force serves as the destabilizing source of the investigated nonlinear dynamical system.

In addition to the physical parameters, a geometrically related aspect ratio defined as $\Gamma = L/d$ should be considered. In this study, we fixed the aspect ratio $\Gamma = 0.614$ corresponding to a half wavelength predicted by linear stability for an infinite fluid layer. The injection strength is also fixed at $C = 10$. Two values of M are considered, i. e. $M = 5$ and $M = 10$.

The non-dimensional boundary conditions specified in Fig. 1 are as follows

$$y = 0 : \Phi = 1, \quad q = 1, \quad u = 0, \quad v = 0, \tag{18}$$

$$y = 1 : \Phi = 0, \quad u = 0, \quad v = 0, \tag{19}$$

$$x = 0, 0.614 : \quad \partial \Phi / \partial x = 0, \quad u = 0, \quad v_x = 0 \quad (free\ walls), \tag{20}$$

$$u = 0, \quad v = 0 \quad (rigid\ walls). \tag{21}$$

Two planar plates (or plane electrodes) separated by a unit length are applied with different voltages. The dielectric liquid subjected to the resulting unipolar injection is investigated since it has many interesting and complex electroconvection phenomena. Two different boundary conditions for lateral walls have been considered. One is the free-slip (symmetrical) boundary condition and the other is the no-slip boundary condition. As for the initial condition, either a rest state or a state obtained from the previous simulation is used in our calculation.

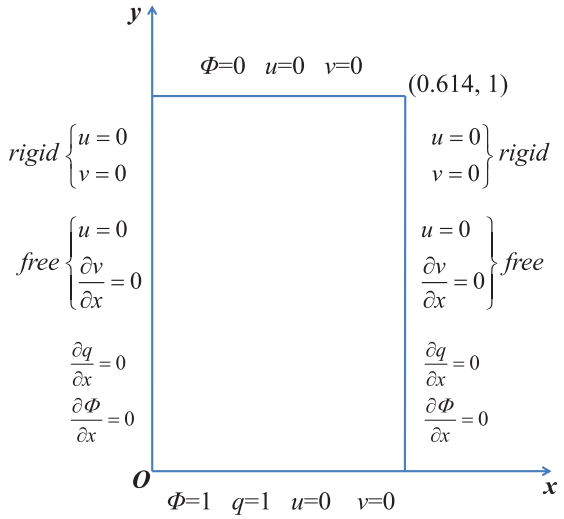

Fig. 1. Schematic of the investigated EHD system.

3. Numerical methods

3.1. Nonlinear simulation

Steep charge density gradients may appear in both weak and strong unipolar injection cases. Application of central difference schemes will result in undesirable over- and under-shoot. While solving the convection–diffusion equation, upwind schemes are generally used under the convection-dominated situation [25]. Owing to small physical diffusion in the charge density transport equation, numerical scheme needs to be stabilized by adding numerical diffusion, which should rapidly vanish as the mesh size goes to zero. There have been numerous methods which have been successfully applied to solve this problem. We adopted another method developed by Chertock et al. [18], which is a hybrid finite-volume finite-difference method for the simulation of a bioconvection (coupled chemotaxis-fluid) system. The bioconvection system is very similar to the present EHD convection system. It is worthy to note that the important feature of this upwind scheme is due to its ability to preserve the positivity property of the computed scalar (charge or cell) density, which can enforce nonlinear stability and is very important to compute non-oscillatory solutions for the charge transport equation [26].

The governing equations are discretized in a staggered Cartesian grid system of uniform mesh size. Chertock et al. [18] used the second-order finite volume upwind method for the scalar transport equations and the second-order centered-difference scheme for the momentum equations cast in vorticity-streamfunction form. Moreover, they used the explicit third-order large-stability-domain Runge–Kutta method (DUMKA3) [27] for time derivative term. In our simulation, the same upwind method is used for charge transport equation, while the momentum equations are solved within the primitive-variable framework, and the Shu-Osher strong-stability-preserving Runge-Kutta method [28] is applied for the time integration.

In order to verify the method adopted to simulate the charge distribution, we have carried out simulations in the hydrostatic regime with different meshes. In the beginning of the computation there is no electric charge in the domain. As time evolves, charges driven by electric field move from the bottom electrode towards the top electrode. When the steady state is reached, the distributions of charge density and electric field admit an analytical solution. The hydrostatic solutions are

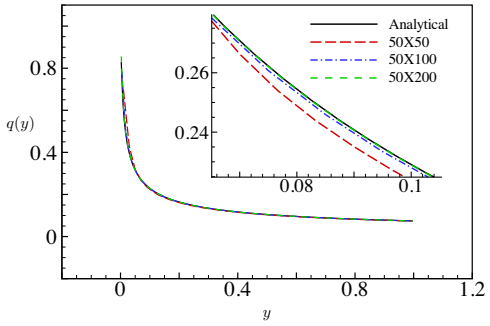

Fig. 2. Charge density along the vertical central line ($x = 0.307$) for the hydrostatic solution when the steady state solution is obtained at $C = 10$ and $M = 10$, $T = 100$. The analytical solution is also plotted for the sake of comparison.

$$q_0(y) = 1/\sqrt{1 + 2Cy/E_s}, \quad E_0(y) = E_s\sqrt{1 + 2Cy/E_s}, \tag{22}$$

where E_s is the electric field at the injector. For each C, it is determined by

$$\int_0^1 E_0(y)dy = 1. \tag{23}$$

The simulated results are compared with the analytical solution shown in Fig. 2. Our results are seen to be in good agreement with analytical solution. The selected charge density profile approaches the analytical one with grid refinement. In the following simulation, a grid of 50 × 100 mesh points is used for the case of small T (near convection threshold) and a grid of 100 × 200 mesh points is employed for the large T case.

3.2. Linear stability analysis

Taking the analytical solutions $q_0(y)$, $\boldsymbol{E}_0 = E_0(y)\boldsymbol{e}_y$ and $\boldsymbol{u}_0 = 0$ as the base solutions, the non-dimensional linearized equations for the perturbation vector $\boldsymbol{S}'(x, y, t)$=($q'(x, y, t)$, $\Phi'(x, y, t)$, $\boldsymbol{E}'(x, y, t)$, $p'(x, y, t)$, $\boldsymbol{u}'(x, y, t)$) read:

$$\nabla^2\Phi' = -Cq', \tag{24}$$

$$\boldsymbol{E}' = -\nabla\Phi', \tag{25}$$

$$\frac{\partial q'}{\partial t} + \nabla\cdot[\ q_0\ (\boldsymbol{E}' + \boldsymbol{u}') + q'\boldsymbol{E}_0\ ] = 0, \tag{26}$$

$$\nabla\cdot\boldsymbol{u}' = 0, \tag{27}$$

$$\frac{\partial \boldsymbol{u}'}{\partial t} = -M^2\nabla\ p' + \frac{M^2}{T}\nabla^2\boldsymbol{u}' + CM^2(\ q_0\ \boldsymbol{E}' + \ q'\ \boldsymbol{E}_0). \tag{28}$$

The linearized equations can be also written as $\partial_t\boldsymbol{S}' = (\mathbf{N}_{\boldsymbol{u}} + \mathbf{L})\boldsymbol{S}'$, where $\mathbf{N}_{\boldsymbol{u}}$ and $\mathbf{L}$ denote the linearized convection and diffusion operators, respectively. When considering $\boldsymbol{S}' = \hat{\boldsymbol{S}}e^{\lambda t}$, the eigenvalue problem given as follows is resulted

$$(\mathbf{N}_{\boldsymbol{u}} + \mathbf{L})\hat{\boldsymbol{S}} = \lambda\hat{\boldsymbol{S}} \tag{29}$$

Instead of directly solving the above eigenvalue problem [9,10], we adopt an alternative approach [29], which enables us to deal with a small matrix representing the action of the Jacobian $(\mathbf{N}_{\boldsymbol{u}} + \mathbf{L})$ on the subspace of leading eigenvectors. The ARPACK [30] library is implemented in this study. The leading eigenvalues and eigenvectors can be accurately obtained at a relatively low computational cost.

Table 1 shows the calculated stability parameter with mesh refinement for the cases with free and rigid walls. For the free wall

Table 1
The critical T values obtained in three meshes from the linear stability analysis.

	64 × 128	100 × 200	128 × 256	Ref. [9]	Ref. [6]	Ref. [10]
Free wall	165.2	164.4	164.1	163.2	164.1	164.1
Rigid wall	351.0	349.3	349.0	340.6	–	349.4

case, our calculated critical T value agrees very well with the results of Atten et al. [6] and Pérez et al. [10] and the converged value is $T_{c,f} = 164.1$. For the rigid wall case, the value obtained under finer grids is $T_{c,r} = 349.0$, which is larger than the result of Wu et al. [9] obtained in coarser grids.

4. Results

The unipolar injection problem under current investigation was mostly studied numerically near the convection threshold. However, its nonlinear development has been less investigated numerically [8]. We are therefore motivated to carry out a detailed numerical simulation of the flow evolving from a rest state to a complex state. Our numerical study of this electroconvection problem will exhibit the presence of some typical bifurcations, such as the pitchfork bifurcation which is transition from one steady flow to another steady flow and associated with the breaking of some symmetry of flow; Hopf bifurcation, indicates that steady flows become time periodic; Quasi-periodic Hopf bifurcation implies transition from periodic state to quasi-periodic state; and heteroclinic bifurcation involves a heteroclinic cycle. Pitchfork and Hopf bifurcations can be identified by the variation of eigenvalues with control parameters. In this work, we do not compute eigenvalues except for the determination of the pitchfork bifurcation for convection threshold. The other bifurcations are all identified by nonlinear simulations.

Simulations are conducted for both free and rigid wall cases. Two mobility parameters, namely $M = 10$ and $M = 5$, are considered in order to study the effect on the nonlinear dynamics. In the following, we have two simulation strategies, one is initiated from a hydrostatic state to get a convective state near the critical T value, Then successively increasing T, and the subsequent simulation is started from previous state at lower T value. The other strategy is to initiate the simulation from a convective state at large T, then successively decreasing T, and the new simulation is started from previous state at higher T value.

4.1. Free wall case

The free-slip (symmetry) boundary conditions for velocity have been applied on two sidewalls.

4.1.1. M=10

Flow development with a successively increasing value of T or decreasing value of T for $M = 10$ is shown firstly in Fig. 3. When increasing the value of T, the primary flow is a static state FS1 as shown in Fig. 4(a). The flow pattern is depicted by a charge density, which exhibits a horizontal uniform distribution and its vertical distribution satisfies the analytical solution given in Eq. (22). The static state loses stability to a one-cell asymmetric steady flow FS2 at $T = 164$, which is in good agreement with that obtained by the linear stability analysis. The charge density and streamlines for FS2 are plotted in Fig. 4(b). Note that the reflection of FS2 flow about the vertical center line is also the solution of the coupled system. Hopf bifurcation occurring at $T = 213$ is accompanied by the generation of a one-cell unsteady flow FS3. This state can be categorized to FS31 and FS32, depending on the different oscillation features. The one-cell oscillating flow obtained at a certain time is plotted in Fig. 4(c). An interesting finding is that when T is increased beyond $T = 281$, a two-cell symmetric steady state FS4 takes its presence. The FS4 state has two convection rolls and they are symmetric with respect to the central mid-plane shown in Fig. 4(d). The two-cell symmetric state loses stability through a Hopf bifurcation at $T = 419$ and a two-cell periodic state FS5 is obtained, meanwhile the reflection symmetry about the vertical mid plane is broken. Similar to the FS3 state, FS5 state is also divided into two states FS51 and FS52. The unsteady two-cell pattern at an instant is drawn in Fig. 4 (e). The chaotic convection state FS6 with a two-cell structure is under our expectation while

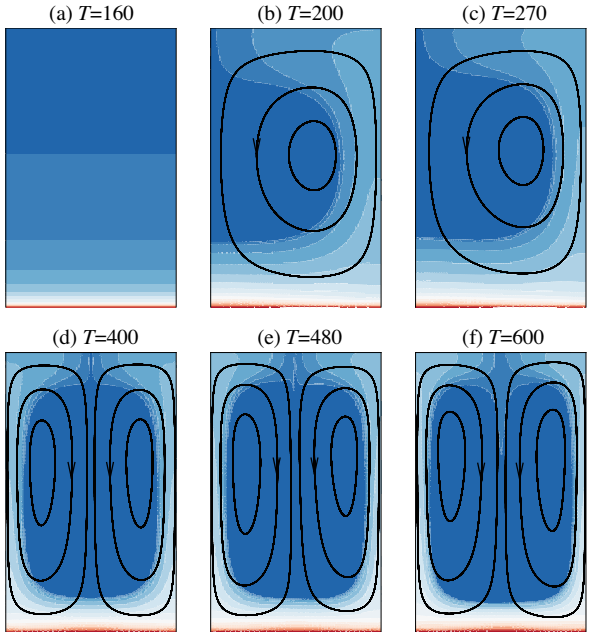

Fig. 4. Distribution of the charge density and streamlines at $M = 10$, and (a) $T = 160$ (FS1); (b) $T = 200$ (FS2); (c) $T = 270$ (FS3); (d) $T = 400$ (FS4); (e) $T = 480$ (FS5); (f) $T = 600$ (FS6). The charge density is plotted from 0.05 to 0.9 with the equal increasing interval 0.05.

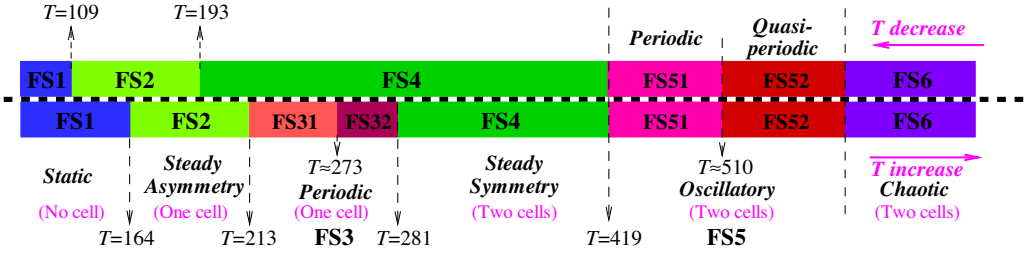

Fig. 3. Schematic of the observed solution branches in different T regions for the free wall case investigated at $M = 10$.

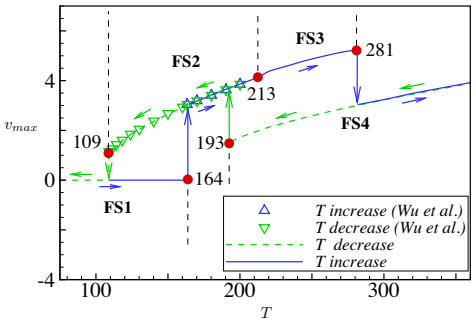

Fig. 5. Bifurcation diagram for T ranging from 75 to 360. The maximum vertical velocity (v_{max}) versus T is drawn. Note that the flow for $213 < T < 281$ is periodic, the time averaged v_{max} is plotted with respect to T. The bullets indicate bifurcation points. The solution branches FS1-FS4 shown in Figure 3 are separated by dashed lines. The symbols denote the results of Wu et al. [9]. (For interpretation of the references to color in this figure legend, the reader is referred to the web version of this article.)

keeping increasing T value. As can be seen from Fig. 4 (f) that the spatial flow structure is regular at the state FS6.

It can be observed from Fig. 4, there is a large region, called the void region, of very low charge density. This void region increases its size with the increasing values of T. The flow states FS1-FS6 qualitatively agree with those of the numerical result of Traoré et al. [8]. However, the FS32 state is not mentioned in their work. As the range of T for FS32 state is small, it is likely to be ignored especially when coarse meshes are used. The present study confirms the results in the literature. More bifurcation information will be given below.

When successively decreasing the T value from the FS6 state, see Fig. 3, the unsteady two-cell flow FS5 is first obtained. As T is decreased below $T = 419$, the two-cell symmetric steady state FS4 is regained. The critical value of T is exactly the same as that obtained in the T-increasing case, indicating that Hopf bifurcation at this point is supercritical. The two-cell symmetric solution FS4 can be sustained until T is decreased to $T = 193$. The solution switches to the one-cell asymmetric steady state FS2 as T is decreased. The comparison of the T-increasing and T-decreasing results around the region of $T = 193 \sim 281$ suggests the appearance of subcritical bifurcations. The flow becomes static with the value of T being further decreased below 109, which is consistent with the previous nonlinear criteria [8,9,17]. Fig. 3 summarizes the bifurcation history in different T regimes for $M = 10$ in free wall case. The co-existence of the multiple flow states at certain T values, the subcritical and supercritical bifurcation phenomena can be observed from the figure. In order to depict more clearly the subcritical feature, the bifurcation diagram is drawn in Fig. 5. The maximum vertical velocity is plotted versus the stability parameter T. Two hysteresis loops can be seen. The first one connects the static state FS1 with the one-cell asymmetric steady state FS2, which has been widely studied before [8,9,17]. This loop is simulated in a 50×100 mesh and the result shows good agreement with the result obtained by Wu et al. [9] (denoted by symbols in the figure). The second one connects the FS2 state with the two-cell symmetric steady state FS4, which has been rarely reported before. This loop is simulated with a finer mesh.

As mentioned before, the unsteady flow pattern FS3 can be classified into two groups, i.e. FS31 and FS32, due to different oscillating natures. In order to illustrate their discrepancy, the time series are plotted in Fig. 6 for $T = 230$ (FS31) and in Fig. 7 for $T = 277$ (FS32). The time series of the charge density at (x, y)=(0.153, 0.25) and the corresponding phase portrait exhibited by (u, v) and the power spectrum density are shown in these two figures. A typical periodic signal can be observed in Fig. 6(a). There is one limit cycle in the phase plot as shown in Fig. 6(b). The

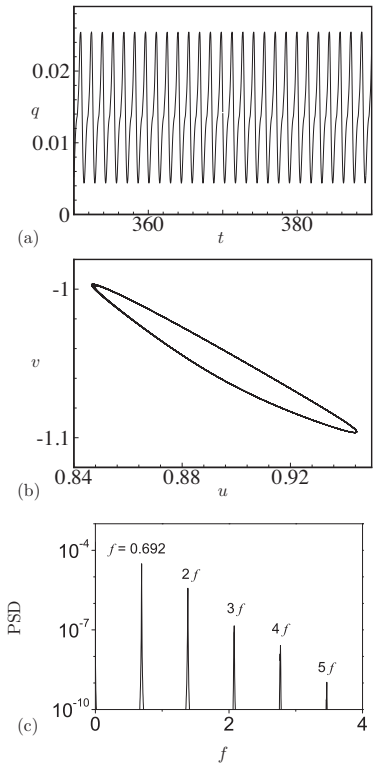

Fig. 6. (a) Illustration the time varying charge density; (b) Phase portrait of (u, v); (c) Power spectrum density (PSD) and (x, y)=(0.153, 0.25) at $T = 230$.

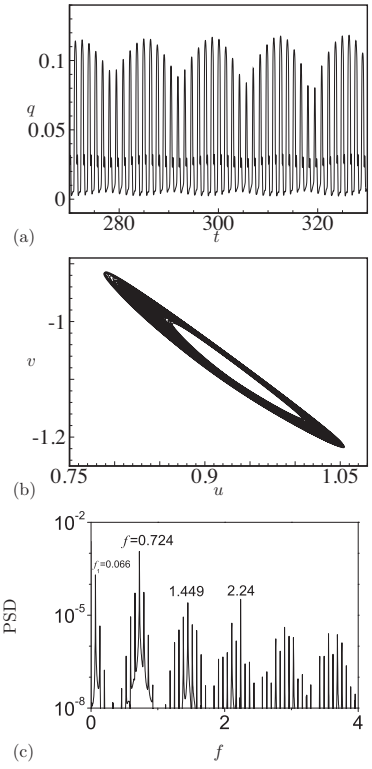

Fig. 7. (a) The calculated time varying solutions; (b) Phase portrait of (u, v); (c) Power spectrum density (PSD) at $T = 277$ and (x, y)=(0.153, 0.25).

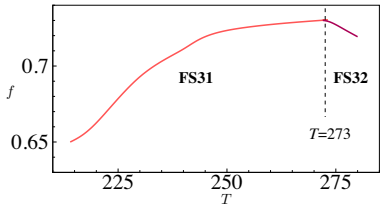

Fig. 8. The dominant frequency of the unsteady state FS3 (see Figure 3) is plotted versus the stability parameter T at $M = 10$ for the free wall case.

power spectrum shown in Fig. 6(c) contains a series of peaks at the primary frequency f and its harmonic frequencies $2f$, $3f$, etc. In contrast, the time series shown in Fig. 7(a) exhibits a modulated behavior. The phase portrait shows a dense toroidal structure as shown in Fig. 7(b), rather than a limit cycle. Moreover, a second periodicity ensues in the system, which is revealed in the power spectrum (Fig. 7(c)) as a second frequency peak at $f_1 = 0.066$ along with the dominant frequency of $f = 0.724$ and other frequencies with smaller contributions. These properties indicate that FS32 has turned into a quasi-periodic state. There exists a transition from a periodic flow to a quasi-periodic flow at $T \approx 273$ via quasi-periodic Hopf bifurcation. Similar bifurcation occurs in the transition from the FS51 state to the FS52 state, whereas there are two cells in the flow. The variation of the dominant frequency f in FS3 state with the stability parameter T is shown in Fig. 8. The frequency increases with the increasing values of T for FS31, and decreases with the increase of T values for FS32.

4.1.2. M=5

The flow bifurcation observed at $M = 5$ for free wall case is shown in Fig. 9. Starting from the static state FS1, we as before successively increase or decrease T in our simulation. The convection (FS3) sets in at $T = 164$, which agrees with the linear stability result. Unlike the $M = 10$ case, the primary convection exhibits however an oscillatory one-cell state rather than a steady state. One explanation for the difference is that the decrease of M results in an increased electric Reynolds number $Re_E = T^2/M$. The inertial effect dominates the viscous effect, leading to the formation of an oscillatory flow. As can be seen from the figure, the oscillatory state FS3 can be also categorized as the FS31 and FS32 states. Two observed quasi-periodic Hopf bifurcations are evidenced by the birth and the disappearance of quasi-periodic flow when increasing the T value. The critical values are respectively predicted to be $T = 231$ and $T = 385$. The periodic flow FS31 becomes the steady FS2 state through an inverse Hopf bifurcation at $T = 1060$. The flow structure for the FS2 state calculated at $M = 5$ is shown in Fig. 10. A large void region is seen to occupy almost the whole cavity, which is much like the charge density distribution in weak injection situation (small C value) [31]. A secondary vortex can be observed at the right lower corner of the cavity at $T = 1200$ (Fig. 10(a)). With the increase of T, new vortex appears at the left upper corner, meanwhile, a small void region is enlarged near the right lower

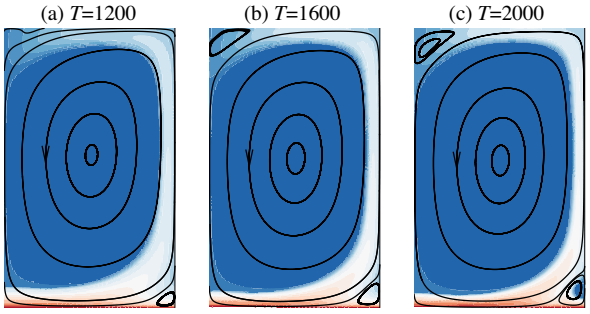

Fig. 10. The patterns of the charge density and streamlines for the FS2 state at $M = 5$, and (a) $T = 1200$; (b) $T = 1600$; (c) $T = 2000$. The charge density is plotted from 0.05 to 0.9 with the equal interval 0.05.

corner. To our surprise, this steady state is found to be stable up to very large T value. Until the largest T=6000 is reached, still the FS2 state is obtained.

When decreasing the value of T from the FS6 state, the steady FS2 state is reached first. Then, the oscillatory state FS3 takes its presence via supercritical bifurcation. The FS3 state is persisted until $T = 157$, where a bifurcation to the one-cell steady state FS2 happens. The steady state FS2 obtained at a low T value, like the case at $M = 10$, suddenly jumps to the motionless state FS1 at $T = 109$. The linear critical value $T = 164$ obtained by increasing the T value and the nonlinear critical value $T = 109$ determined by decreasing T are the same to those of $M = 10$, thereby confirming that the critical T value near the convection threshold does not depend on the mobility parameter M [6].

It is interesting to note here that the flows obtained with either successively increasing the T value from the rest state or decreasing the T value from the chaotic state are all of the one-cell type as shown in Fig. 9. Another simulation was performed by taking the static state as the initial condition and we perform simulation at $T = 800$. A chaotic state with the two-cell structure similar to the FS6 state at $M = 10$ is obtained. Take the FS6 state as the initial condition, we successively decrease T value and plot the bifurcation diagram in Fig. 11. The two-cell periodic state FS51 and the two-cell steady symmetry state FS4 are obtained sequentially. The FS4 state loses stability to the periodic state FS31 at $T = 191$. The bifurcation sequences under the further decrease of T values are almost the same as that shown in Fig. 9.

4.2. Rigid wall case

It is always interesting to compare the simulated results of the rigid wall case with that of the free wall case, including the linear stability [8–10] and the numerical simulation results. However, the discrepancy of the nonlinear evolution between these two cases has been rarely reported.

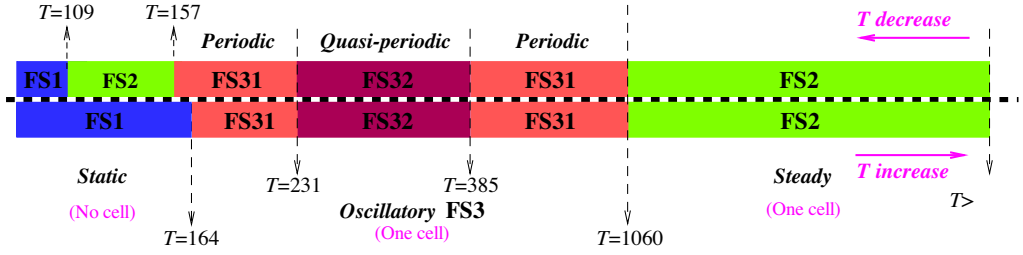

Fig. 9. Illustration of the obtained solution branches in different T regions for the free wall case with $M = 5$.

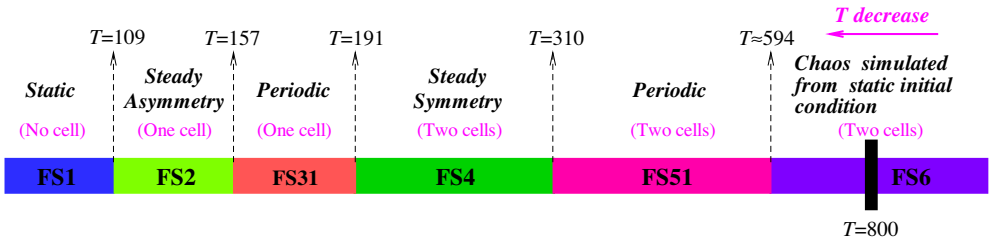

Fig. 11. Illustration of the simulated solution branches in different T regions for the free wall case with $M = 5$. Note that the simulation procedure starts with calculating one state with the static initial condition at $T = 800$, then we continuously decrease the T values from this state.

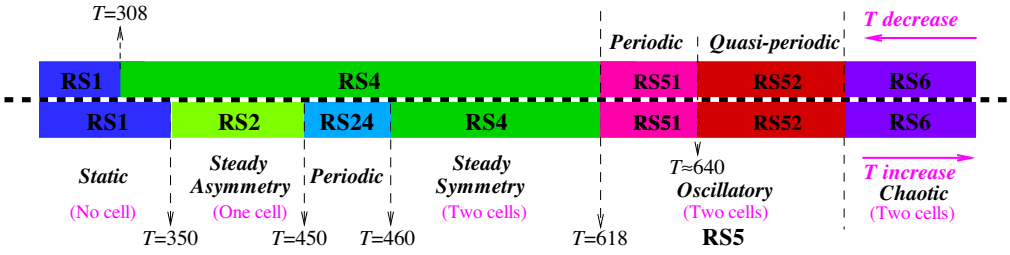

Fig. 12. Illustration of the simulated solution branches in different T regions for the rigid wall case with $M = 10$. Note that RS24 represents a transient state, and the flow pattern in this region is oscillating between the one-cell structure and the two-cell structure.

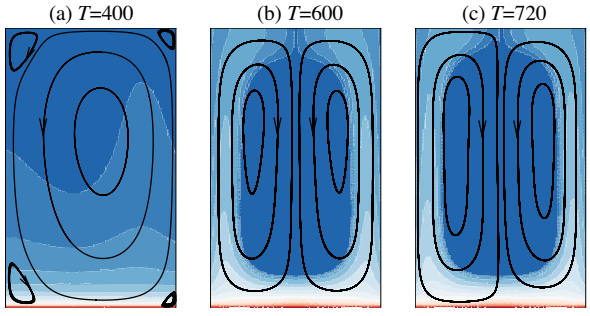

Fig. 13. Distribution of the charge density and streamlines for $M = 10$, and (a) $T = 400$; (b) $T = 600$; (c) $T = 720$. The charge density is plotted from 0.05 to 0.9 with the equal interval 0.05.

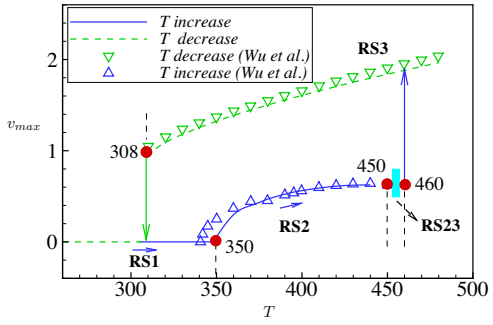

Fig. 14. Bifurcation diagram for T ranging from 260 to 500. The maximum vertical velocity (v_{max}) versus T is drawn. The bullets indicate the bifurcation points. The solution branches RS1, RS2, RS4 and RS24 shown in Figure 12 are separated by the dashed lines. The symbols denote the results of Wu et al. [9]. (For interpretation of the references to color in this figure legend, the reader is referred to the web version of this article.)

4.2.1. M=10

The solution branches obtained by either increasing or decreasing the T values for $M = 10$ (rigid wall case) are schematically shown in Fig. 12. The static state RS1 is obtained first at a small T, which is the same as the FS1 state for the free wall case. Flow convection sets in with the increasing T values. The critical T value obtained from the numerical simulation is 350, which is in agreement with that by the linear stability analysis in Section 3.2. The flow structure is characterized by the existence of one main cell located at the center and other four small cells near the corners as shown in Fig. 13 (a). This RS2 pattern is much complex than the one-cell pattern FS2 for the free wall case due to the no-slip wall effect. As can be seen from the figure, the distribution of charge density is quite different from that of the free wall case. The transport of ions near the lateral walls is resisted by the zero velocity at the walls. With T being further increased, in contrast to the periodic one-cell FS3 state in the free wall case, a transient oscillatory RS24 state is found and it will be discussed later. By keeping increasing the T value, we obtained the steady two-cell symmetric state RS4, the periodic two-cell state RS5 and the quasi-periodic or chaotic state RS6. The critical T values for the transition are labeled in Fig. 12. The symmetric flow RS4 is shown in Fig. 13(b) at $T = 600$ and the asymmetric pattern is shown in Fig. 13(c) at $T = 720$. The counterparts of the three states for the free wall case are FS4, FS5 and FS6, respectively. When decreasing the values of T from the RS6 state, RS5 and RS4 states are obtained sequentially under expectation. Whereas, the RS4 state is sustained until $T = 308$. The static state is regained for the case with a smaller T value.

The bifurcation diagram for T from 260 to 500 is shown in Fig. 14. Similar to that in the free wall case, the bifurcation phenomenon near the convection threshold was also reported [8,9]. It is shown in the figure that the bifurcation for the onset of convection is supercritical, whereas the bifurcation from the one-cell pattern RS2 to the two-cell pattern RS4 is subcritical. There exists a hysteresis loop linking the static state RS1 with the steady two-cell state RS4. The results of Wu et al. [9] are also plotted in the figure for comparison. Note that Wu et al. also studied the nonlinear evolution of flow for T ranging from 360 to 460. However, the transient state RS24 was not revealed in their work.

The transient state RS24 is actually periodic as shown in Fig. 15(a). The period for this flow is much larger than that in the FS3 flow observed in free wall case. The flow feature is inherently different as well. The contours of the charge density and streamlines at the four times labeled in Fig. 15(a) are plotted in Fig. 15(b).

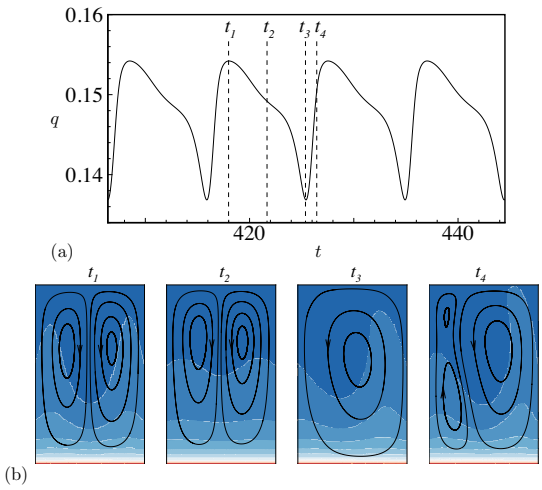

Fig. 15. (a) The simulated time varying charge density at $(x, y) = (0.153, 0.25)$ for $T = 458$; (b) Distribution of the charge density and streamlines at four distinct times $t_1 - t_4$ labeled in (a). The charge density is plotted from 0.05 to 0.9 under the equal interval 0.05.

A two-cell flow similar to RS4 state shown in Fig. 13(b) is observed at t_1. The flow gradually evolves to a one-cell pattern similar to that in the RS2 state shown in Fig. 13(a) at t_3. The splitting from the one-cell structure to two cells can be seen at t_4. The flow at t_4 will develop into a two-cell structure at t_1 again, completing the periodic oscillation. The flow properties at the RS24 state imply the presence of a heteroclinic orbit. The heteroclinic connections have been widely studied in plane Couette flow [32], channel flow [33], pipe flow [34], and in von Kármán swirling flow, but are rarely reported in EHD flow.

4.2.2. M=5

The flow evolutions either with increasing or decreasing T for $M = 5$ are demonstrated in Fig. 16. Many similar features to those of the $M = 10$ case can be observed. The critical T values for the supercritical and subcritical bifurcations near the onset of convection are identical to the values for $M = 10$ case, which are 350 and 308. This indicates that for the rigid wall case, the onset of convection is also independent of the mobility parameter M [6]. The flow states RS1, RS2, RS24, RS5, RS6 described above for $M = 10$ are all found here. However, the steady symmetric two-cell state RS4 is not observed. When decreasing the T value, the hysteresis loop is characterized by the periodic state RS5 rather than by the steady state RS4. It is worthy to note here that the critical T value for the transition to quasi-periodic or chaotic flow is much smaller than that for the case obtained at $M = 10$.

5. Conclusion

The electroconvective flow of dielectric liquid in a cavity subjected to unipolar injection is investigated numerically. The nonlinear EHD equations have been solved using the finite volume method which is second order accurate both in time and in space. The verification study shows that the current numerical approach can satisfactorily simulate the electroconvection. Both of the free and rigid lateral conditions have been considered in our study. The effects of the mobility parameter on the nonlinear flow evolution are also evaluated.

For the free wall and $M = 10$ case, the FS1, FS2, FS3, FS4, FS5 and FS6 states are observed numerically one after the other while continuously increasing T from the rest state, as shown in Fig. 3. When decreasing the T value from the chaotic state FS6, the sequence of the flow states FS6, FS5, FS4, FS2, FS1 occurs. The disappearance of FS3 state is due to subcritical bifurcation. The transition to chaotic flow is through the quasi-periodic route.

For the free wall and $M = 5$ case, two simulation strategies using different initial conditions have been employed. The first one is similar to the $M = 10$ case which starts from the state obtained from a previous simulation. Under this circumstance, the FS1, FS3 and FS2 states are obtained sequentially when continuously increasing the T values from the rest state, and FS2, FS3, FS2, FS1 appear one by one when continuously decreasing T from the chaotic state (see Fig. 9). All the flows are featured with the one-cell structure. The primary convective flow is periodic rather than steady. The second simulation strategy starts from the rest state at a large T value, and the two-cell chaotic state is obtained. The subsequent simulations are based on this two-cell state by continuously decreasing T values until the static state is regained. The FS51 (two-cell), FS4 (two-cell), FS31 (one-cell), FS2 (one-cell) states appear one after the other (see Fig. 11).

For the rigid wall and $M = 10$ case (see Fig. 12), the order of the appearance of flow states in accordance with increasing T is RS1, RS2, RS24, RS4, RS5, RS6, and the order for the case with the decreasing T values is RS6, RS5, RS4, RS1. Compared with the free wall case, the one-cell periodic state is not found but the new oscillatory state with a larger period RS24 is obtained, which is regarded as a heteroclinic orbit.

For the rigid wall and $M = 5$ case (see Fig. 16), the bifurcation sequence is almost the same as that of the $M = 10$ case. The major difference is that the two-cell steady symmetric state RS4 is no longer existing. The hysteresis loop near the convection threshold is linked by the two-cell periodic flow RS5. It is interesting to note that the two-cell steady asymmetric state is never obtained in all our simulations, no matter what lateral wall boundary condition is considered.

Overall, rich bifurcations and nonlinear dynamics have been studied in great detail in a geometrically very simple EHD system. Unlike the bifurcation and instability near the convection threshold which are predictable and less affected by the mobility param-

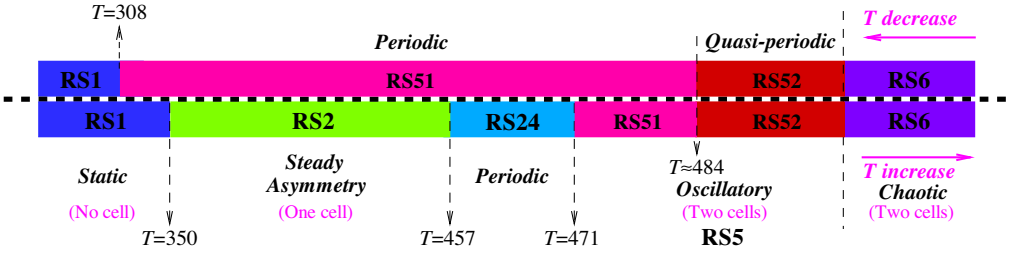

Fig. 16. Illustration of the calculated solution branches in different T regions for the rigid wall case with $M = 5$. Note that RS24 represents a transient state, and the flow pattern in this region is oscillating between the one-cell structure and the two-cell structure.

eter, flow transition in nonlinear regime depends on the mobility parameter and requires a careful numerical study. The initial condition as well has an influence on the nonlinear developing flow pattern, especially for the free wall and the low mobility parameter cases.

Acknowledgments

This research is supported by MOST (Ministry of Science and Technology) through the Grants NSC 98-2628-M-002-006 and 98-2811-E-002-006. This research is also supported by Natural Science Foundation of China under Grant No 11502137.

References

[1] J.M. Cowley (Ed.) Fundamentals of Applied Electrostatics, Wiely New York, 1986.
[2] Vázquez PA, Georghiou GE, Castellanos C. Characterization of injection instabilities in electrohydrodynamics by numerical modelling: comparison of particle in cell and flux corrected transport methods for electroconvection between two plates. J Phy D: Appl Phys 2006;39:2754.
[3] Vázquez PA, Perez AT, Castellanos A, Atten P. Dynamics of electrodynamic laminar planes: scaling analysis and integral model. Phys Fluids 2000;12:2809.
[4] Castellanos A. Injection induced instability and chaos in electrohydrodynamics. J Phy Condens Matt 1990;2:SA499.
[5] Schneider JM, Watson PK. Electrohydrodynamic stability of space-charge-limited currents in dielectric liquids. I. Theoretical study. Phys Fluids 1970;13:1948.
[6] Atten P, Moreau R. Stabilité electrodynamique des liquides isolants soumis á une injection unipolaire. J Mécanique 1972;11:471.
[7] Atten P, Lacroix JC. Nonlinear hydrodynamic stability of liquids subjected to unipolar. J de Méc 1979;16:469.
[8] Traoré P, Pérez AT. Two-dimensional numerical analysis of electroconvection in a dielectric liquid subjected to strong unipolar injection. Phys Fluids 2012;24:037102.
[9] Wu J, Traoré P, Vázquez PA, Pérez AT. Onset of convection in a finite two-dimensional container due to unipolar injection of ions. Phys Rev E 2013;88:053018.
[10] Pérez AT, Vázquez PA, Wu J, Traore P. Electrohydrodynamic linear stability analysis of dielectric liquids subjected to unipolar injection in a rectangular enclosure with rigid sidewalls. J Fluid Mech 2014;758:586.
[11] Atten P, Lacroix JC, Malraison B. Chaotic motion in a coulomb force driven instability: large aspect ratio experiments. Phys Lett A 1980;79:255–8.
[12] Malraison B, Atten P. Chaotic behavior of instability due to unipolar ion injection in a dielectric liquid. Phys Rev Lett 1982;49:723.
[13] Castellanos A, Atten P, Pérez AT. Finite amplitude electroconvection in liquids in the case of weak unipolar injections. Physico-Chem Hydrodyn 1987;9:443–52.
[14] Chicón R, Castellanos A, Martin E. Numerical modelling of Coulomb-driven convection in insulating liquids. J Fluid Mech 1997;344:43–66.
[15] Pérez AT, Castellanos A. Role of charge diffusion in finite-amplitude electroconvection. Phys Lett A 1989;40:5844–55.
[16] Vázquez PA, Georghiou GE, Castellanos A. Numerical analysis of the stability of the electrohydrodynamic (ehd) electroconvection between two plates. J Phy D: Appl Phys 2008;41:175303.
[17] Vázquez PA, Castellanos A. Numerical simulation of EHD flows using discontinuous Galerkin finite element methods. Comput Fluids 2013;84:270–8.
[18] Chertock A, Fellner K, Kurganov A, Lorz A, Markowich PA. Sinking, merging and stationary plumes in a coupled chemotaxis-fluid model: a high-resolution numerical approach. J Fluid Mech 2012;694:155–90.
[19] Castellanos A, editor. Electrohydrodynamics. New York: Springer; 1998.
[20] Atten P. Electrohydrodynamic instability and motion induced by injected space charge in insulating liquids. IEEE Trans Dielectr Electr Insul 1996;3:1–17.
[21] Melcher JR, editor. Continuum Electromechanics. Massachussets, US: MIT Press; 1981.
[22] Landau LM, Lifshitz EM, editors. Electrodynamics of continuous media. New York: Pergamon; 1984.
[23] Rodriguez-Luis A, Castellanos A, Richardson AT. Stationary instability in a dielectric liquid layer subjected to an arbitrary unipolar injection and an adverse thermal gradient. J Phy D: Appl Phys 1986;19:2115–22.
[24] Pontiga F, Castellanos A. The onset of overstable motions in a layer of dielectric liquid subjected to the simultaneous action of a weak unipolar injection of charge and a thermal gradient. Q J Mech Appl Math 1992;45:25–46.
[25] LeVeque RJ, editor. Finite volume methods for hyperbolic problems. Cambridge: Cambridge University Press; 2002.
[26] Chertock A, Kurganov A. A second-order positivity preserving central-upwind scheme for chemotaxis and haptotaxis models. Numer Math 2008;111:169–205.
[27] Medovikov AA. High order explicit methods for parabolic equations. BIT 1998;38:372–90.
[28] Shu C-W, Osher S. Efficient implementation of essentially non-oscillatory shock-capturing schemes. J Comput Phys 1998;77:439–71.
[29] Tuckerman LS, Barkley D. Bifurcation analysis for time-steppers 2000;119:453–66.
[30] Lehoucq RB, Sorensen DC, Yang C, editors. ARPACK users guide: solution of large-scale eigenvalue problems with implicitly restarted Arnoldi methods. Philadelphia, PA: SIAM; 1998.
[31] Traoré P, Wu J. On the limitation of imposed velocity field strategy for Coulomb-driven electroconvection flow simulations. J Fluid Mech 2013;727:R3.
[32] Halcrow J, Gibson JF, Cvitanović P, Viswanath D. Heteroclinic connections in plane Couette flow. J Fluid Mech 2009;621:365–76.
[33] Toh S, Itano T. A periodic-like solution in channel flow. J Fluid Mech 2003;481:67–76.
[34] Duguet Y, Willis AP, Kerswell RR. Transition in pipe flow: the saddle structure on the boundary of turbulence. J Fluid Mech 2008;613:255–74.